Bioprocess and Biosystems Engineering
https://doi.org/10.1007/s00449-024-03112-2

RESEARCH PAPER

Computational fluid particle dynamics modeling of tangential flow filtration in perfusion cell culture

Hamideh Hayati[1] · Caitlin Kurtz[2] · Yu Feng[1] · Sarwat Khattak[2]

Received: 16 August 2024 / Accepted: 19 November 2024

Abstract

Membrane fouling is a common and complex challenge with cell culture perfusion process in biopharmaceutical manufacturing that can have detrimental effects on the process performance. In this study, we evaluated a method to calculate the hollow fiber membrane resistance at different time points for water and supernatant. In addition, the number of subvisible particles of < 200 nm. diameter suspended in the supernatant were quantified using a nano-flow cytometry method. A computational fluid dynamics (CFD) model was developed to evaluate the impact of feed flow rate and particle count on the transmembrane pressure (TMP). Then a steady-state discrete phase model was applied to incorporate particles into the model and simulate the particles deposition over the membrane wall. The results showed an increase in the number of particles and the membrane resistance along the time course of the perfusion process. The CFD model illustrated that more particle deposition was observed at lower feed stream flow rates. The fraction of deposited particle was reduced by > 50% when the feed flow rate was increased from 35 ml/min to 300 ml/min. Our findings suggest that the total number of subvisible particles has a significant impact on TMP and membrane resistance and, thus, could play a major role in the mechanism of membrane fouling. CFD modeling can be a useful tool to predict the behavior of a process in a specific membrane. CFD simulations could also be used to optimize process parameters to improve membrane cleanability, reduce particle deposition, and reduce the risk of membrane fouling.

Keywords Computational fluid particle dynamics (CFPD) · Tangential flow filtration (TFF) · Extracellular vesicles · Cell culture · Perfusion · Hollow fiber filter

Abbreviations

Acronyms

ATF	Alternating tangential flow filtration
BCs	Boundary conditions
CAD	Computer-aided design
CFPD	Computational fluid particle dynamics
CHO	Chinese hamster ovary
DF	Deposition fraction
EVs	Extracellular vesicles
FTh	Fiber thickness
ID	Lumen inner diameter
lm	Lumen
LL	Lumen length
NL	Number of lumens
SA	Lumen surface area
TFF	Tangential flow filtration
TMP	Transmembrane pressure

Symbols

$\vec{F}^{BM}$	Brownian motion-induced force
$\vec{F}^{D}$	Drag force
$\vec{F}^{G}$	Gravity
$\vec{F}^{P}$	Pressure-gradient force
$\vec{F}^{vm}$	Virtual mass force
g_i	Gravity in i-direction
m_p	Particle mass
P_F	Feed flow pressure
P_P	Permeate flow pressure
P_R	Retentate flow pressure
p	Local fluid pressure
R	Porous media resistance
S	Momentum sink by porous media

✉ Caitlin Kurtz
caitlin.kurtz@biogen.com

[1] School of Chemical Engineering, Oklahoma State University, Stillwater, OK 74078, USA

[2] Cell Culture Development, Biogen, 5000 Davis Drive, Research Triangle Park, NC 27709, USA

Published online: 03 January 2025

$\vec{u}_p$ Particle velocity
v_i Local fluid velocity in i-direction

Greek symbols

α Porous media permeability
μ Fluid viscosity
ρ Fluid density

Introduction

Advances in the biopharmaceutical industry have led to the need for greater volumes and concentrations of mammalian cell culture to produce recombinant biological byproducts, i.e., monoclonal antibodies [1, 2]. Perfusion cell culture systems are currently of high interest because of their potential to intensify the process, increase facility throughput, and produce a consistent product quality of therapeutic proteins [1–8].

Several perfusion technologies have been developed for both the production and the seed bioreactor stages. Filtration systems based on tangential flow filtration (TFF) and alternating flow filtration (ATF) have been the most widely used in industry for their ability to support very high cell density perfusion cell culture processes and integrate bioreactor and product clarification operations into a single unit process [9, 10]. The ATF hollow fiber-based perfusion system is estimated to be the most cost-effective compared to fed-batch and spin filter perfusion systems [11]. However, one major drawback that is still limiting widespread adoption of hollow fiber filtration systems is membrane fouling and product retention [8, 12–18]. Membrane fouling is an irreversible process and is generally associated with the build-up of cells, cell debris, and extracellular material at the membrane surface or within its pores [13, 19].

The perfusion process discussed in this study is based on a TFF process in the N−1 seed train stage. The N−1 perfusion process goal is to exceed the cell mass that can be achieved in a batch or fed-batch mode using a cell retention device to continuously remove metabolic waste from the culture and replacing it with fresh media. A high cell density N−1 culture enables higher initial cell density in the subsequent production bioreactor stage, with the potential to increase volumetric productivities and shorten the overall production stage. This approach has been utilized in various forms across the industry with many documented improvements in product quality, facility utilization, and batch to batch consistency [2, 20, 21]. In the TFF process, the cell culture is removed from the N−1 bioreactor using a positive displacement pump and pushed through the hollow fiber filters in a single flow direction. The cells or the retentate are returned to the bioreactor in a recirculating loop while the permeate is removed from the retentate tangential to the direction of the flow. The TFF systems rely on the flow of the cell culture fluid inside the hollow fibers to generate liquid shear to clear gel layer formation on the filter surface and minimize fouling [22–25]. While higher shear results in better cleaning and potentially less fouling, it can also negatively impact cell viability [18, 26, 27]. Strategies to mitigate the risk of filter fouling aimed to avoid the release of membrane foulants originating from cell lysis in the first place, either by increasing the concentration of shear protectants [28] or by reducing the mechanical shear stress caused by recirculating pumps for cell culture [18, 29, 30]. Wang et al. [18] suggested that particles of approximately 100 nm size range in the perfusion cell culture are responsible for product sieving and membrane fouling in TFF membranes. Pinto et al. [31] demonstrated a 100% sieving efficiency by substituting the microporous 0.2 µm pore-size membrane filters with macroporous membranes of pore size range from 1 to 4 µm. In our N−1 development work, we observed different levels of membrane fouling across different programs and host cell lines. The goal of this work is to analyze the cell culture broth from various cell culture programs to understand how its composition impacts the membrane resistance, and to identify correlations between the number and size of suspended particles in the subvisible size range to the risk of membrane fouling in these processes.

Extracellular vesicles (EVs) are produced by most cell types, including mammalian cell lines such as Chinese hamster ovary (CHO) cells which are the most used cell line for producing biotherapeutics. EVs are believed to constitute a major fraction of all suspended particles in the cell culture broth. EVs range in size from nano- to macro- and are lipid bound vesicles that are secreted by the cell into the extracellular environment to serve a variety of cell specific functions including cell-to-cell communication.

As interest in EVs across the industry has grown because of their potential use as biomarkers and therapeutic applications [32–34], investment into improved methods for analysis and quantification of EVs has followed. Physical analysis of EVs to measure their concentration within a sample and to capture the size distribution of these particles can be determined directly through high-resolution imaging or indirectly through optical or electrical measures as reviewed by Hartjes et al. [35]. Scanning electron microscopy, transmission electron microscopy, atomic force microscopy, dynamic light scattering, nanoparticle tracking analysis, tunable resistive pulse sensing, and flow cytometry are the most common methods used for EV size determination. In this study, we used the nano-flow cytometry method to determine the concentration and size distribution of the EV particles identified in our cell culture retentate fluid stream.

Fluid flow simulation in cell culture perfusion filters using computational fluid dynamics has been applied to ATF systems in a simplistic 2D model and has been proven successful

to provide evidence of the starling flow phenomenon which has been hypothesized but difficult to prove practically [36]. The model also showed a visual understanding of membrane utilization during different phases of ATF cycles. This work provided the motive for our current study to develop a more advanced 3D CFD model for our TFF process to understand how different cell culture broth compositions and process parameters impact the fluid flow behavior in the filtration process. Moreover, by incorporating the experimental data provided from particle size analysis into our CFD model, we developed a computational fluid particle dynamics (CFPD) model to provide a comparative visualization for particle deposition on the filter membrane at different process operating parameters. To our knowledge, this is the first time to utilize CFPD model to simulate cell culture perfusion processes. The model we present is one step toward developing a model that could simulate particle deposition on membrane surface and predict filter fouling, and hence, guide process decisions like membrane selection, cell line/clone selection, and process parameter set points.

Governing equations

An experimentally validated one-way CFPD model was employed to simulate subvisible particle transport and deposition in cell culture TFF process. Particles were assumed to be spherical with no particle–particle interaction. The computational domain had two zones: a fluid zone and a porous zone. The governing equations for the fluid zone, porous zone, and particle transport are described in the following subsections.

Fluid flow

Based on the flow rates used in the experiments, the flow regime stays laminar throughout the hollow fiber filter. Continuity and Navier–Stokes equations for steady state, Newtonian, incompressible flow are defined as [37]:

$$\frac{\partial v_x}{\partial x}+\frac{\partial v_y}{\partial y}+\frac{\partial v_z}{\partial z}=0 \tag{1}$$

$$\begin{aligned} v_x\frac{\partial v_x}{\partial x}+v_y\frac{\partial v_x}{\partial y}+v_z\frac{\partial v_x}{\partial z} \\ =-\frac{1}{\rho}\frac{\partial P}{\partial x}+\frac{\mu}{\rho}\left(\frac{\partial^2 v_x}{\partial x^2}+\frac{\partial^2 v_x}{\partial y^2}+\frac{\partial^2 v_x}{\partial z^2}\right) \\ +g_x+S, \end{aligned} \tag{2}$$

where v_i is the local fluid velocity in *i-direction*. The terms on the right hand side of the Navier–Stokes equation denote pressure force, viscous force, and gravitational force on an element per unit volume of fluid, respectively. In this study, thermodynamic properties of supernatant were assumed to be equal to those of water with density (ρ) = 998.2 kg/m^3 and viscosity (μ) = 1.55e−3 kg/m s. Although Eq. (2) is only depicted in x-direction, the equation was solved in y- and z-directions as well, since the computational domain is three dimensional. The last term S represents momentum sink by the porous media.

Porous media

In porous media, momentum sink is equal to transmembrane pressure (TMP) along the depth of the membrane. Based on Darcy's law [38], TMP is proportionate to permeate velocity (v) by the porous media permeability (α).

$$S=\mathrm{TMP}=-\frac{\mu}{\alpha}v. \tag{3}$$

Porous media permeability is the reciprocal of its resistance (R):

$$\alpha=\frac{1}{R} \tag{4}$$

TMP is defined by [39]:

$$\mathrm{TMP}=\frac{P_F+P_R}{2}-P_P, \tag{5}$$

where P_F, P_R, and P_P are feed flow, retentate flow, and permeate flow pressures, respectively. TMP value is used to calculate membrane resistance. (Please refer to "Hollow fiber membranes" section to see how TMP is measured through experiments). The values of calculated resistance are presented in Table 1.

Particle transport

Particles traveling with fluid flow are subjected to different forces. To obtain the trajectory of particles, particle equation of motion (Newton's Second Law) was solved, which is defined as [40, 41]:

$$\frac{d}{dt}\left(m_p\vec{u}_p\right)=\vec{F}^D+\vec{F}^L+\vec{F}^{BM}+\vec{F}^G+\vec{F}^P+\vec{F}^{vm}, \tag{6}$$

where m_p and $\vec{u}_p$ are particle mass and velocity. $\vec{F}^D$ is the drag force [42], $\vec{F}^L$ is the Saffman lift force [43], and $\vec{F}^{BM}$ is the Brownian motion-induced force [40]. The terms $\vec{F}^G$ and $\vec{F}^P$ are the particle gravity and pressure-gradient force, respectively, while $\vec{F}^{vm}$ is the virtual mass force [44].

Table 1 Porous media (hollow fiber) properties and boundary conditions

Porous media		
Viscous resistance[a] ($1/m^2$)		Inertial resistance[b] (1/m)
Water 4.18e + 14	Supernatant 4.32e + 15	0
Boundary conditions		
Boundaries	Discrete phase BCs type	Fluid BCs type
Lumen inlet (water/supernatant)	Escape	Velocity inlet
Retentate region–porous media interface	Trap	Porous jump
Porous media–permeate region interface	–	Interface
Permeate region walls	–	No slip
Permeate and retentate flow outlets	Escape	Pressure outlet

[a] Measured by experiments as presented in "Materials and methods" section

[b] Inertial resistance is zero for laminar flows

Table 2 Characteristic dimensions of hollow fiber filter

Material	NL	LL(m)	SA (m^2)	ID (m)	FTh (m)
Polysulfone	10	0.6	1.75e−2	1e−3	[2.58e−4, 3.12e−4]

Boundary conditions

Boundary conditions (BCs) used for the simulations are listed in Table 1 [38]. The inner surface of the porous zone was considered porous (known as porous jump) with an infinite face permeability ($1e + 20\ m^2$) to allow particles to deposit while the fluid passes through the porous media to the permeate region.

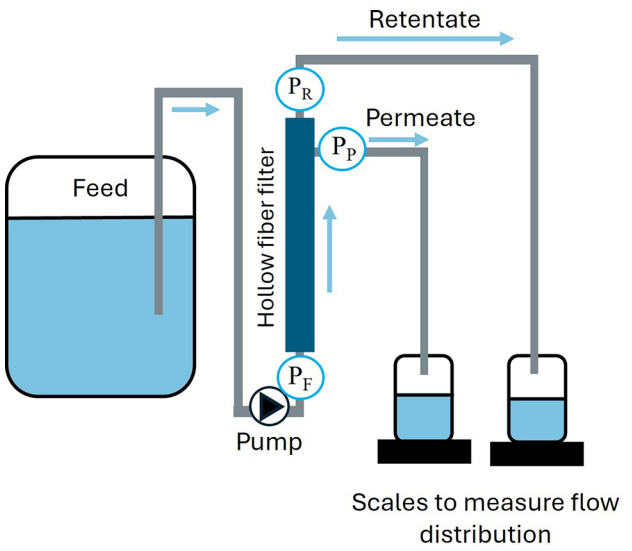

Fig. 1 Experimental setup for membrane resistance measurement

Materials and methods

For CFPD simulation of hollow fiber filters, filter resistance (R) value is needed as an input. For calculating R, multiple experiments were performed with both water and cell-free supernatant (i.e., serum-free cell culture spent medium) as the feed flow. In the following sections, experimental and computational set-ups are elaborated.

Hollow fiber membranes

Characteristic dimensions of the hollow fiber filter for TFF (number of lumens (NL), lumen length (LL), lumen surface area (SA), lumen inner diameter (ID), and fiber thickness (FTh)) are presented in Table 2.

Membrane resistance measurement

Membrane resistance was measured by flowing deionized water and cell-free supernatant (serum-free media) through the hollow fiber membrane at three rates (67, 115, and 230 ml/min). The hollow fiber filter was configured in a vertical orientation with the lower permeate port blocked off. Experimental setup is demonstrated in Fig. 1. Pressures, retentate weight, and permeate weight were recorded at 1-min intervals for 3 min to calculate transmembrane pressure (TMP) and membrane resistance (R) using Eqs. (3–5).

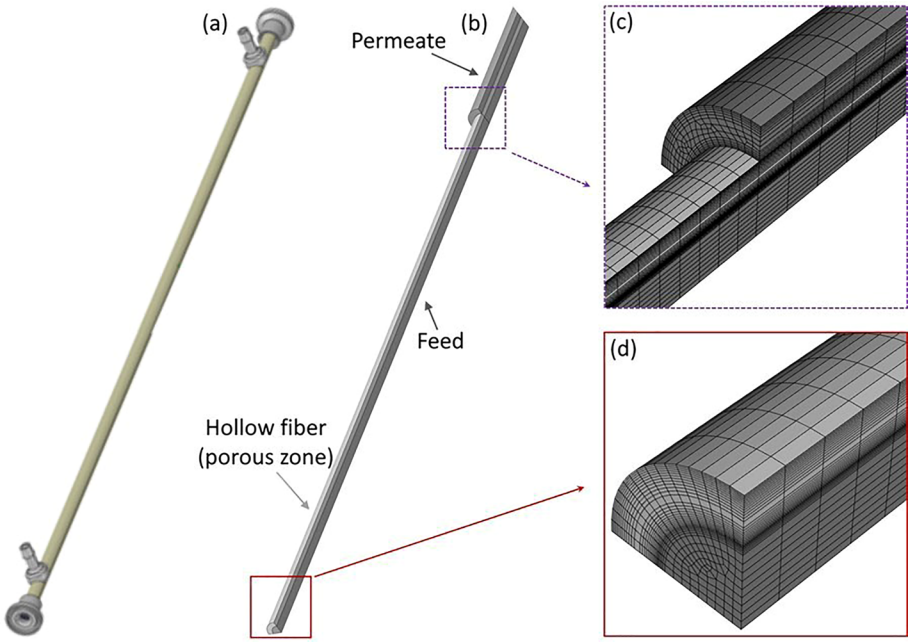

Fig. 2 Hollow fiber filter geometry and mesh: **a** 10-lm hollow fiber filter geometry; **b** reconstructed geometry of one quarter of the single lumen with symmetry planes. Up-close snapshot of the structured mesh at **c** inlet region and **d** the region where filtration starts (the first and last 3.3 cm of the permeate region were sealed so no computational domain was considered for those regions)

Subvisible particle analysis

Daily samples were collected from five CHO cell culture processes producing different therapeutic monoclonal antibodies. The samples were centrifuged to separate cells, and the cell culture supernatant was analyzed by the nano-flow cytometry (NanoFCM, Xiamen, China) for particle concentration, size distribution, and surface protein marker phenotyping as described in literature [45–47]. For this analysis, two single photon counting avalanche photodiodes (APDs) were used for simultaneous detection of side scatter (SSC) and individual particles fluorescence. The instrument calibration was performed for particle concentration and size distribution using 200 nm PE and AF488 fluorophore conjugated polystyrene beads and Silica Nanosphere Cocktail (NanoFCM Inc., S16M-Exo), respectively. Particles passing by the detector during a 1-min interval were recorded in each test, and all samples were diluted to achieve a particle count within a 2000–12,000/min range. The flow rate and side scattering intensity were converted into corresponding vesicle concentration and size on the NanoFCM software (NanoFCM Profession V1.0).

Numerical solution

An experimentally validated Euler–Lagrange CFPD [48] model was used to simulate particle transport/deposition in the TFF model.

Hollow fiber filter geometry reconstruction and mesh generation

The three dimensional 10-lm CAD model for the filter unit employed for the current study is shown in Fig. 2a, provided by Meissner (Camarillo, CA). After multiple simulations, it was observed that fluid dynamics is identical in all lumens. Therefore, only one of the lumens was studied in the current work. Fluid velocity in directions perpendicular to the main flow direction was assumed zero and the fluid was considered isothermal throughout the domain. Hence, there is no normal temperature, velocity, or acceleration gradient on the mid-planes along the main flow inside the lumen and fiber and the permeate flow. Therefore, only one quarter of the lumen was simulated, and symmetry boundary condition was employed. The computational model comprises three regions: feed (water or supernatant); hollow fiber (porous zone); and permeate. Figure 2b shows the reconstructed one quarter of a single lumen. The characteristic dimensions of the model can be seen in Table 2.

The finite volume mesh was generated using Ansys Meshing 2022 R2 (ANSYS Inc., Canonsburg, PA). After performing mesh independence test, the final mesh contained 1,347,900 hexahedron-based cells (feed, hollow fiber, and permeate domains were meshed by 300,900, 708,000, and 339,000 elements, respectively). High-gradient regions (near-wall and near-interface regions) were covered by five layers of prism elements to precisely capture near-wall effects. Surface elements are shown in Fig. 2c and d.

Single-phase flow numerical setup

Ansys Fluent 2022 R2 was used for the fluid field analysis, and the flow was assumed steady state. Fluid flow was simulated for three different particle-free water and supernatant flow rates (67, 115, and 230 ml/min). Boundary conditions and flow rates are reported in Table 1. Viscous resistance value, obtained from the experimental data, was 4.18e + 14 $1/m^2$ for water and 4.32e + 15 $1/m^2$ for supernatant. The inertial resistance was considered zero since the flow was laminar [38].

Particle flow

One-way coupled Euler–Lagrange method was used for particle tracking. It was assumed that particles are spherical and particle–particle interaction was neglected. After fluid analysis finished, particles with the diameter of 70 nm were injected into the lumen from the inlet.

Results and discussion

Model validation

The CFD model was validated by running simulations at feed (water) flow rates of 67, 115, and 230 ml/min. Experimental resistance values obtained from water testing of 10-lm hollow fiber filter ($n = 5$) were used to run CFD simulations. In Fig. 3, TMP and flow distribution for water through the hollow fiber filter are compared. CFD model validation using membrane resistance values obtained from water testing of the membrane indicated that the model could accurately predict TMP as well as the permeate and retentate flow rates as all model predictions were within the experimental ranges. As expected, it is shown in Fig. 3a that TMP increased with increasing feed flowrate. However, the ratio between permeate and retentate flowrates remains constant at approximately 80% retentate to 20% permeate at all tested water flowrates as it could be depicted from Fig. 3b and c.

Single-phase fluid flow

Velocity contours of flow inside the porous media (v_p) and pressure contours inside the lumen (P_F) and in the permeate region (P_P) at a mid-plane of the hollow fiber filter are demonstrated in Fig. 4. The contours show that the hollow fiber is not fully utilized for filtration, which is because the pressure gradient between P_F and P_P declines gradually as the feed moves in the axial direction. Pressure difference and v_p in the outlet region are nearly zero. Furthermore, increasing the feed inlet flow rate from 67 ml/min to 230 ml/min did not enhance the membrane utilization. This can be also seen in Fig. 5, which shows the permeate flow velocity contours on outer surface of the fiber (in permeate region) at the inlet, middle, and outlet areas of the filter for three different water flow rates. Permeate velocity has its highest value at inlet region for all three flowrates and it decreases moving toward the middle region and it becomes 0 m/s in the outlet region of the filter. These observations suggest that increasing inlet flow rates does not necessarily improve the filter efficiency/functionality.

These results reported in Figs. 3, 4, and 5 agree with findings from Radoniqi et al. [36], where their 2D CFD model predicted only 50% membrane utilization for permeate flow for each pressure and exhaust phase of the ATF cycle. In their computational study, this percent was not impacted by changing the feed flow rate within their tested range. The results from our model suggest that varying the geometry or the number of lumens in a hollow fiber filter unit could be a viable option to alter velocity gradient in a TFF process and improve membrane efficiency.

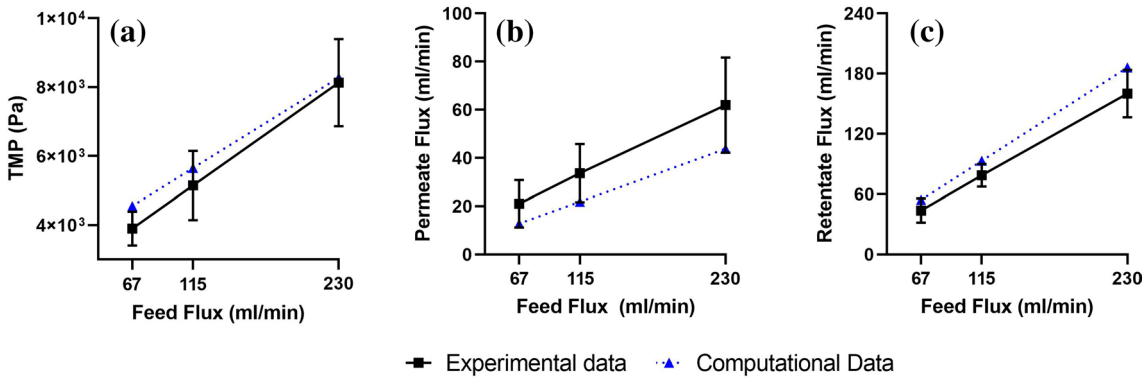

Fig. 3 Computational model validation for water as the feed: comparison of values obtained by experiments and CFD simulations for **a** transmembrane pressure (TMP); **b** permeate flow; and **c** retentate flow**.** Error bars represent one standard deviation around the experimental data results ($n = 5$)

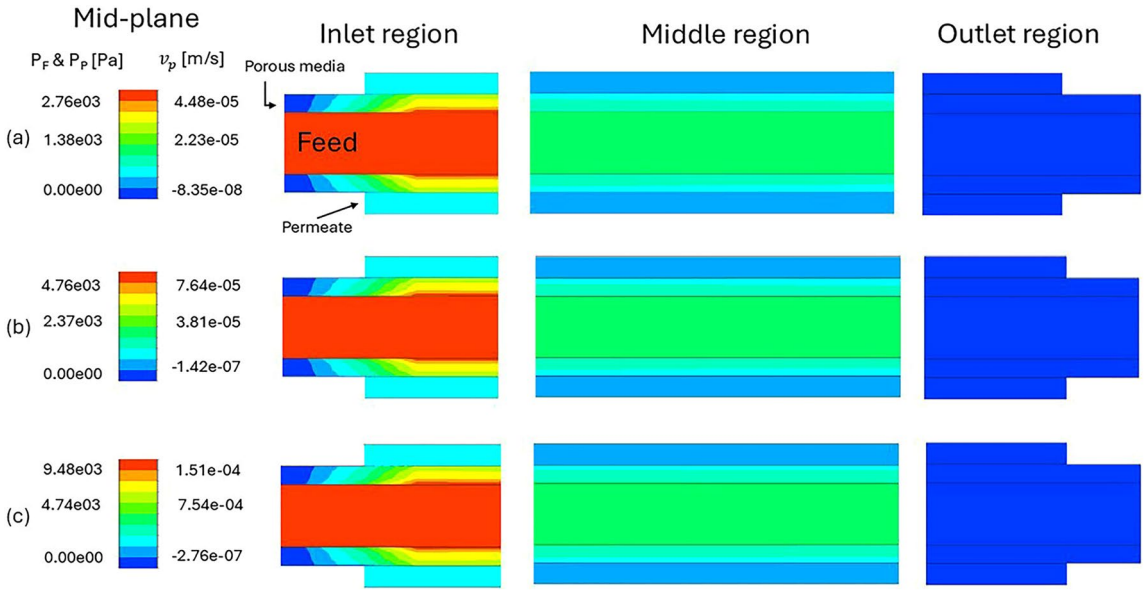

Fig. 4 Mid-plane pressure (P_F and P_P) contour and velocity contour of the flow inside the fiber (v_p) in inlet, middle, and outlet regions for feed (water) flux of **a** $Q_F = 67$ ml/min; **b** $Q_F = 115$ ml/min; and **c** $Q_F = 230$ ml/min

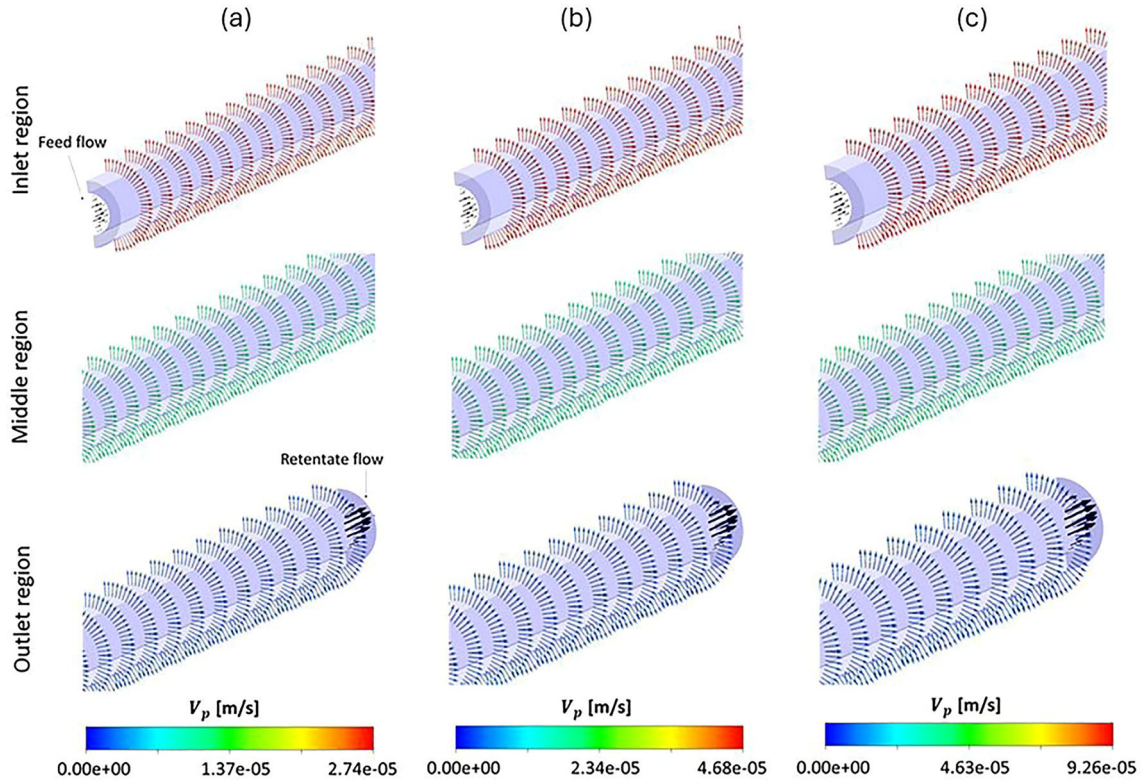

Fig. 5 Permeate flow velocity vectors on outer surface of the fiber (in permeate region) in inlet, middle, and outlet area of the filter for different water flux at **a** $Q_F = 67$ ml/min; **b** $Q_F = 115$ ml/min; and **c** $Q_F = 230$ ml/min

Supernatant flow

The CFD model was employed for simulating supernatant flow through the filter. Figure 6 shows TMP and flow distribution obtained by both computational simulations and experiments for supernatant flow. The resistance value

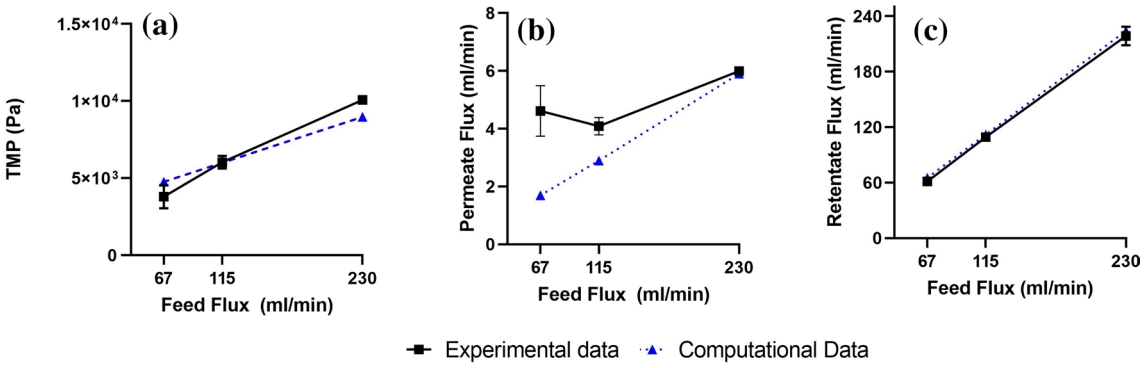

Fig. 6 Computational and experimental data of **a** transmembrane pressure (TMP); **b** permeate flow; and **c** retentate flow for supernatant feed. Error bars represents one standard deviation around the experimental data results ($n=2$)

$R=4.32e+15\ 1/m^2$ obtained from supernatant experiments was used for CFD simulations (n = 2). The flow distribution and TMP obtained by experimental and computational tests are in good agreement. Similar to the results from water feed simulations, TMP value increases when supernatant flux increases (Fig. 6a). The filter's higher resistance for supernatant leads to a lower permeate flow and a higher retentate flow (Fig. 6a, b) compared to water (Fig. 3). As shown in Fig. 6b, less than 2 ml/min of permeate flux was reported by CFD analysis when $Q_F=67$ ml/min, which is less than 3% of the total feed flux. This ratio remains constant when inlet flow rate increases up to $Q_F=230$ ml/min. Since the experiments were run at cell-free supernatant, the higher resistance for the supernatant flow, compared to water, resulting in low filtration rate could be attributed to extracellular fluid particle deposition on the inner surface of the hollow fiber and reducing the membrane efficiency. Therefore, particle analysis in the cell culture broth is performed to identify, quantify, and simulate their deposition on the filter membrane.

Particle flow analysis

The validated CFD model was used to predict particle transport/deposition in the hollow fiber filter. Simulating the flow of the total number of particles detected in the supernatant via subvisible particle analysis would be challenging in terms of computational power and time. Therefore, a particle tracking test with smaller number of particles was performed to examine if particle deposition fraction (DF) is independent of the initial number of particles (NPC). As shown in Fig. 7a, for different inlet feed flowrates ranging from $Q_F=35$ ml/min to $Q_F=300$ ml/min, deposition fraction magnitude plateaus for initial NPC larger than 8000. Reducing the initial NPC from 5,200,000 to 8000 per lumen dropped particle tracking time from 116 h to about 6 min for $Q_F=300$ ml/min. Therefore, simulating 8000 particles/lumen is considered sufficient to predict particle DF. Deposition fraction of particles versus feed flux Q_F is plotted in Fig. 7b, and it shows that increasing flow rate from $Q_F=35$ ml/min to $Q_F=115$ ml/min resulted in a sharp

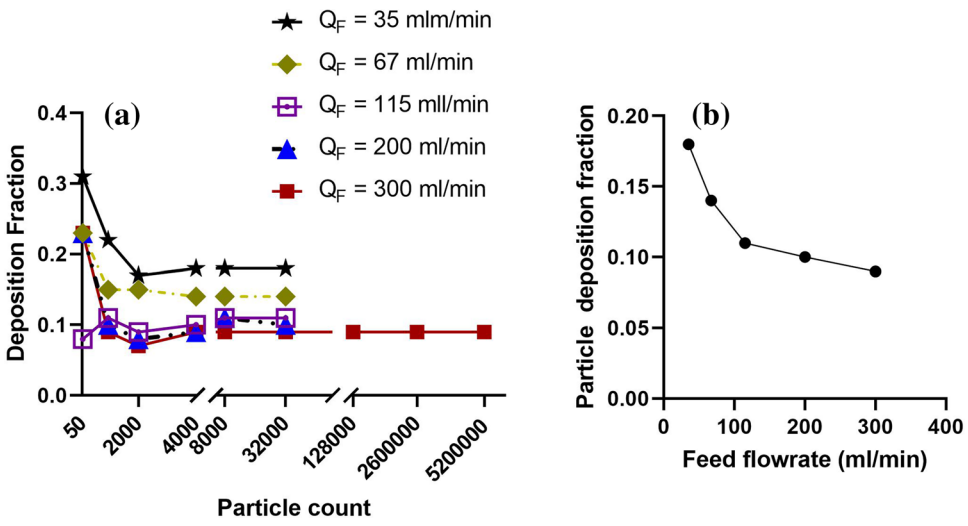

Fig. 7 Particle depositions fraction (DF) for different inlet feed flowrates Q_F: **a** comparison of particle DF for different initial particle count suspended in feed flows with different Q_F; and **b** particle DF for different inlet flowrates Q_F

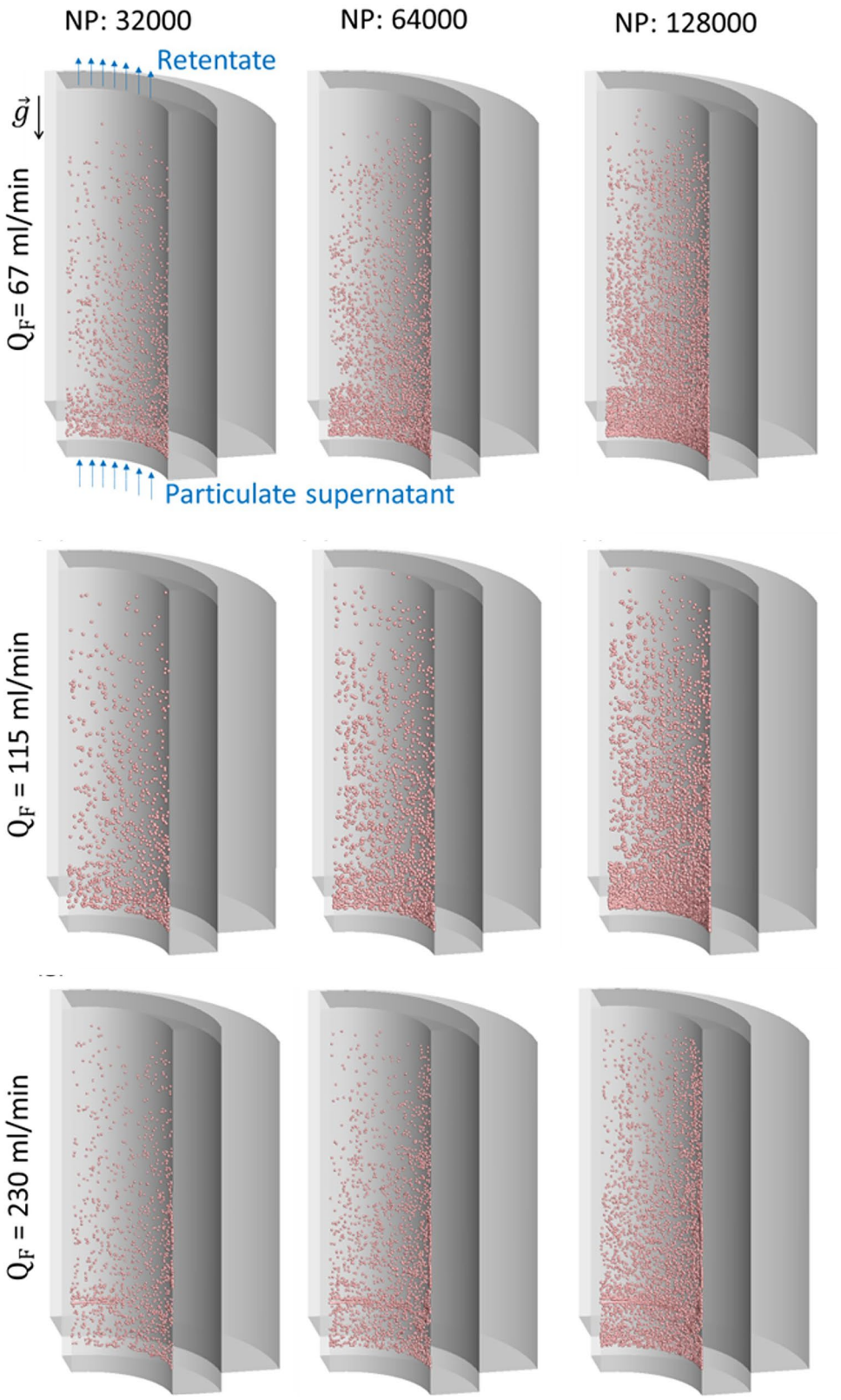

Fig. 8 A visualization of deposited particles of different particle counts (NPC = 32,000, 64,000, and 128,000) for feed flow rates of **a**–**c** $Q_F = 67$ ml/min; **d**–**f** $Q_F = 115$ ml/min; and **g**–**i** $Q_F = 230$ ml/min

reduction in total particle deposition from 18 to 11% while a further increase in flow rate up to $Q_F = 300$ ml/min only reduced the deposition fraction by 2%. These results could be attributed to the fact that higher flow rates result in a lower particle residence time and hence a lower risk of particle deposition and filter fouling. The correlation between

flow rate and particle deposition fraction, however, is not linear, which suggests that to select an optimum flow rate for a specific process, it is important to find the right balance between enhanced filter cleanability at higher flow rates and its potential negative impact from increased shear stress on cells.

Visualizing deposited particles on the inner surface of the hollow fiber could provide a better understanding of filter fouling mechanisms. In Fig. 8, local deposition of particles is visualized for different initial NP with different flow rates. For all three flow rates, i.e., $Q_F = 67$ ml/min (Fig. 7a–c), $Q_F = 115$ ml/min (Fig. 7d–f), and $Q_F = 230$ ml/min (Fig. 7g–i), particles tend to deposit less as traveling from the inlet region toward to the outlet region. This could be explained by the higher TMP in the inlet region than in the outlet region leading to a larger pressure gradient that forces the particles toward the membrane surface at the beginning of the lumen. Furthermore, the particle number density of the deposited particles for higher flow rates ($Q_F = 300$ ml/min) is less than that for lower ($Q_F = 67$ ml/min), which suggests that higher flowrates could provide better cleanability for the membranes.

Conclusion

Filter fouling in cell culture perfusion is a well-known and complex problem that is not completely understood. To our knowledge, this study is the first attempt to utilize a multiphase 3D CFD model to simulate fluid flow in hollow fiber filters and predict the pattern of subvisible particle deposition on the membrane wall. The study also provides experimental methods that can be applied to make perfusion process-related decisions. For instance, measuring the membrane resistance, as described in this study, for various membrane chemistries, pore sizes, vendors, or lots can help in identifying filter membranes with lower resistance that may reduce the risk of membrane fouling and improve the filtration robustness of the perfusion process. Moreover, EVs quantification and particle size analysis techniques could be a powerful tool to select host cell lines or clones that are low EVs producers, and hence become better candidates for programs intended for continuous manufacturing or N−1 perfusion. Lastly, while the CFD model provided in this study has its limitations for not considering particle–particle interaction or particle accumulation on the membrane wall in a transient simulation to mimic the fouling process, it provides good insights on membrane utilization and the pattern of particle deposition on the membrane surface. The model results could be used to investigate potential improvements in hollow fiber geometries to allow better membrane utilization and more efficient filtration, and to guide development activities around optimizing process flowrates to mitigate risk of filter fouling. Further improvements in the model to incorporate a discrete element model to describe the particle interactions and the cake layer formation in a transient simulation is possible but requires more computational power and further simplifications to the model.

Acknowledgements We gratefully acknowledge our collaboration with Meissner and would specifically like to acknowledge Thomas Lazzara and Mark Morgan for providing valuable expertise in filtration and membrane technology, membrane resistance measurement and for providing the original hollow fiber CAD model. We would like to acknowledge Dr. Momen Amer for his expertise in computation fluid dynamics and his contributions to the CFPD model development. We would like to express our sincere gratitude for his dedication and support throughout this research project and for his constructive comments that greatly enhanced the quality of this manuscript.

Data included in this study are available upon request by contact with the corresponding author.

Author contributions All authors contributed to the study conception and design. CFPD analysis and modeling were performed by Hamideh Hayati. The first draft of the manuscript was written by Hamideh Hayati. Material preparation, data collection, and experimental execution related to hollow fiber membranes, membrane resistance, and subvisible particle analysis that served as inputs to the CFPD model was performed by Caitlin Kurtz. Yu Feng provided the UDF codes used in the analysis and reviewed the manuscript. Sarwat Khattak supervised the project and reviewed the manuscript. All authors commented on previous versions of the manuscript. All authors read and approved the final manuscript.

Funding This study was funded by Biogen Inc.

Data availability Data included in this study are available upon request by contact with the corresponding author.

Declarations

Conflict of interest The authors have no competing interests to declare that are relevant to the content of this article.

References

1. Bielser J-M et al (2018) Perfusion mammalian cell culture for recombinant protein manufacturing—a critical review. Biotechnol Adv 36(4):1328–1340
2. Yang WC et al (2014) Perfusion seed cultures improve biopharmaceutical fed-batch production capacity and product quality. Biotechnol Prog 30(3):616–625
3. Doane A et al (2016) Implementation of a recirculating TFF N-1 perfusion system at manufacturing scale: conquering process hurdles and scaling challenges. In: Cell culture engineering XV, Robert Kiss, Genentech Sarah Harcum, Clemson University Jeff Chalmers, Ohio State University Eds, ECI Symposium Series. https://dc.engconfintl.org/cellculture_xv/24
4. Pollock J et al (2017) Integrated continuous bioprocessing: economic, operational, and environmental feasibility for clinical and commercial antibody manufacture. Biotechnol Prog 33(4):854–866

5. Rodrigues ME et al (2010) Technological progresses in monoclonal antibody production systems. Biotechnol Prog 26(2):332–351
6. Su WW (2009) Bioreactors, perfusion. In: Flickinger MC (ed) Encyclopedia of industrial biotechnology: bioprocess, bioseparation, and cell technology, vol 1. John Wiley & Sons, pp 1–17. https://doi.org/10.1002/9780470054581.eib149
7. Warikoo V et al (2012) Integrated continuous production of recombinant therapeutic proteins. Biotechnol Bioeng 109(12):3018–3029
8. Zydney AL (2016) Continuous downstream processing for high value biological products: a review. Biotechnol Bioeng 113(3):465–475
9. Clincke MF et al (2013) Very high density of CHO cells in perfusion by ATF or TFF in WAVE bioreactor™. Part I. Effect of the cell density on the process. Biotechnol Prog 29(3):754–767
10. Godawat R et al (2015) End-to-end integrated fully continuous production of recombinant monoclonal antibodies. J Biotechnol 213(suppl C):13–19
11. Pollock J et al (2013) Fed-batch and perfusion culture processes: economic, environmental, and operational feasibility under uncertainty. Biotechnol Bioeng 110(1):206–219
12. Bolton GR, Apostolidis AJ (2017) Mechanistic modeling of the loss of protein sieving due to internal and external fouling of microfilters. Biotechnol Prog 33(5):1323–1333
13. Chew JW, Kilduff J, Belfort G (2020) The behavior of suspensions and macromolecular solutions in crossflow microfiltration: an update. J Membr Sci 601:117865
14. Clincke MF et al (2013) Very high density of Chinese hamster ovary cells in perfusion by alternating tangential flow or tangential flow filtration in WAVE bioreactor™—part II: applications for antibody production and cryopreservation. Biotechnol Prog 29(3):768–777
15. Karst DJ et al (2017) Process performance and product quality in an integrated continuous antibody production process. Biotechnol Bioeng 114(2):298–307
16. Kim M, Zydney AL (2006) Theoretical analysis of particle trajectories and sieving in a two-dimensional cross-flow filtration system. J Membr Sci 281(1–2):666–675
17. Kim S-C et al (2016) Effect of transmembrane pressure on Factor VIII yield in ATF perfusion culture for the production of recombinant human Factor VIII co-expressed with von Willebrand factor. Cytotechnology 68(5):1687–1696
18. Wang S et al (2017) Shear contributions to cell culture performance and product recovery in ATF and TFF perfusion systems. J Biotechnol 246:52–60
19. Field R (2010) Fundamentals of fouling. Membr Water Treat 4:1–23
20. Padawer I, Ling WLW, Bai Y (2013) Case study: an accelerated 8-day monoclonal antibody production process based on high seeding densities. Biotechnol Prog 29(3):829–832
21. Woodgate JM (2018) Perfusion N-1 culture—opportunities for process intensification. Biopharmaceutical processing. Elsevier, pp 755–768
22. Velez D et al (1989) Use of tangential flow filtration in perfusion propagation of hybridoma cells for production of monoclonal antibodies. Biotechnol Bioeng 33(7):938–940
23. Maiorella B et al (1991) Crossflow microfiltration of animal cells. Biotechnol Bioeng 37(2):121–126
24. Mercille S et al (1994) Filtration-based perfusion of hybridoma cultures in protein-free medium: reduction of membrane fouling by medium supplementation with DNase I. Biotechnol Bioeng 43(9):833–846
25. Van Reis R et al (1997) High performance tangential flow filtration. Biotechnol Bioeng 56(1):71–82
26. Johnstone P et al (2020) Development of a small-scale rotary lobe-pump cell culture model for examining cell damage in large-scale N-1 seed perfusion process. Biotechnol Prog 36(6):e3044
27. Amer M et al (2022) Evaluating shear in perfusion rotary lobe pump using nanoparticle aggregates and computational fluid dynamics. Bioprocess Biosyst Eng 45(9):1477–1488
28. Xu S et al (2017) Impact of Pluronic® F68 on hollow fiber filter-based perfusion culture performance. Bioprocess Biosyst Eng 40(9):1317–1326
29. Blaschczok K et al (2013) Investigations on mechanical stress caused to CHO suspension cells by standard and single-use pumps. Chem Ing Tech 85(1–2):144–152
30. Karst DJ et al (2016) Characterization and comparison of ATF and TFF in stirred bioreactors for continuous mammalian cell culture processes. Biochem Eng J 110:17–26
31. Pinto ND et al (2020) Impact of micro and macroporous TFF membranes on product sieving and chromatography loading for perfusion cell culture. Biotechnol Bioeng 117(1):117–124
32. Colombo M et al (2014) Biogenesis, secretion, and intercellular interactions of exosomes and other extracellular vesicles. Annu Rev Cell Dev Biol 30:255–289
33. Bank IE et al (2015) The diagnostic and prognostic potential of plasma extracellular vesicles for cardiovascular disease. Expert Rev Mol Diagn 15(12):1577–1588
34. Quek C, Hill AF (2017) The role of extracellular vesicles in neurodegenerative diseases. Biochem Biophys Res Commun 483(4):1178–1186
35. Hartjes TA et al (2019) Extracellular vesicle quantification and characterization: common methods and emerging approaches. Bioengineering 6(1):7
36. Radoniqi F et al (2018) Computational fluid dynamic modeling of alternating tangential flow filtration for perfusion cell culture. Biotechnol Bioeng 115(11):2751–2759
37. Bird RB, Steward WE, Lightfoot EN (1960) Transport phenomena. Wiley, New York
38. Jackson GW, James DF (1986) The permeability of fibrous porous media. Can J Chem Eng 64:364–374
39. Stressmann M, Moresoli C (2008) Effect of pore size, shear rate, and harvest time during the constant permeate flux microfiltration of CHO cell culture supernatant. Biotechnol Prog 24(4):890–897
40. Hayati H et al (2019) Numerical modeling of particle motion and deposiiton in turbulent wavy channel flows. Sci Iran 26(4):2229–2240
41. Hayati H, Feng Y, Hinsdale M (2021) Inter-species variabilities of droplet transport, size change, and deposition in human and rat respiratory systems: an in silico study. J Aerosol Sci 154:105761
42. Chen X et al (2017) Numerical investigation of the interaction, transport and deposition of multicomponent droplets in a simple mouth-throat model. J Aerosol Sci 105:108–127
43. Saffman PG (1965) The lift on a small sphere in a slow shear flow. J Fluid Mech 22(2):385–400
44. Kolev NI (2010) Multiphase flow dynamics 2, mechanical interaction, 4th edn. Springer
45. Dong L et al (2020) Comprehensive evaluation of methods for small extracellular vesicles separation from human plasma, urine and cell culture medium. J Extracell Vesicles 10(2):e12044
46. Zhu S et al (2014) Light-scattering detection below the level of single fluorescent molecules for high-resolution characterization of functional nanoparticles. ACS Nano 8(10):10998–11006
47. Tian Y et al (2018) Protein profiling and sizing of extracellular vesicles from colorectal cancer patients via flow cytometry. ACS Nano 12(1):671–680
48. Hayati H, Feng Y, Hinsdale M (2021) Inter-species variabilities of droplet transport, size change, and deposition in human and rat respiratory systems: an in silico study. J Aerosol Sci 154:1–22